

Scattering from a finite cylinder near an interface

John A. Fawcett

DRDC - Atlantic Research Centre, PO Box 1012,

Dartmouth, N.S., Canada, B2Y 3Z7

john.fawcett@drdc-rddc.gc.ca

April 28, 2014

Received:

Running Title: Scattering from a finite cylinder

Abstract

In this paper a Boundary Integral Equation Method (BIEM) is described for the computation of scattering from a finite, rigid, cylinder near a pressure-release interface. The cylinder lies parallel or tilted with respect to the interface plane so that the azimuthal symmetry of the problem is destroyed. The scattering solution is first described in terms of an azimuthally-symmetric free space solution. The multiple interactions of the scattered field with the interface are accounted for by an azimuthal-conversion matrix. In the numerical examples, the method of this paper is benchmarked using wavefield superposition for a sphere near a pressure-release surface. Computed scattered spectra are shown for a finite cylinder, parallel and tilted with respect to the interface, and for a variety of source/receiver geometries. The differences resulting from not including multiple target/interface interactions (single scatter solution) and from including all interactions are presented. The problem of irregular frequencies for the single-scatter and the fully coupled BIEM are discussed and numerically examined.

PACS numbers: 43.20.Fn, 43.30.Gv

I. INTRODUCTION

The numerical solution of scattering from objects near or on an interface has been described¹⁻⁶ by previous authors. In Refs. 4 and 5, the scattering was solved using a finite-element code. For some geometries, such as a sphere or a vertically-oriented cylinder near an interface, the scattering problem can be solved as a sequence of azimuthal problems (i.e., the Fourier components are uncoupled). For a cylinder lying parallel or tilted with respect to the interface, the azimuthal symmetry is broken and one utilizes either a single-scattering solution or a full three-dimensional solution⁵. The single-scattering solution is an approximate solution where the effects of the interface are accounted for with respect to the incident field and also in the propagation of the field, computed on the surface of the cylinder, to a receiver(s). For the single-scatter approach the solution upon the target's surface can still be computed with an uncoupled azimuthal expansion method. The accuracy of the single scatter solution has been explored by various authors^{2,6} and although, it is often a very good approximation, it is also inaccurate for certain scenarios. This paper will consider the accuracy of the single-scatter approximation for different monostatic scattering angles and different orientations of a rigid target near a pressure-release surface. A flat-ended cylinder, tilted or parallel to the interface, serves as an interesting test case for the single-scatter approximation. The scattering will consist of both specular and diffraction returns. As well, for a tilted cylinder, there can be significant target/interface interactions for certain geometries.

The solution method, Boundary Integral Equation Method (BIEM), using Fourier expansions is first described for the free space problem^{7,8}. Next, a finite, rigid cylinder below a pressure release surface is considered. In this case, the concept of an image cylinder is introduced and a conversion matrix, describing the conversion of the solution upon this image cylinder into a field re-incident upon the physical cylinder is

derived. This conversion matrix can be ignored in the BIEM system of equations (leading to the single-scatter solution), can be included iteratively, or a fully-coupled system of equations (all orders of interactions) can be solved. For the cylinder lying parallel to the interface, a computationally efficient method for computing the conversion matrix is derived. For a cylinder tilted with respect to the interface, the conversion matrix is somewhat more difficult to compute.

In the Numerical Examples section, the case of a sphere lying below a reflecting interface is first considered as a benchmark case. With respect to the vertical axis, the problem is azimuthally symmetric and we solve it with a virtual source method^{9–11} using the appropriate half-space Green's function. However, we also consider the Fourier expansion about the horizontal axis and use the cylindrical BIEM with a conversion matrix. Next, using the BIEM technique, a finite cylinder lying parallel to the interface is considered. The spectra for the scattered fields are computed for 3 monstatic angles using the single-scatter and full-interaction solutions, and the differences are discussed. The irregular frequencies^{7,8,12} of the single-scatter and full multiple-scatter solutions are investigated. Finally, a cylinder tilted at -45° with respect to the horizontal is considered. Once again, the single- and full-scattering solutions are computed for 3 monstatic angles and the spectra and corresponding time series computations discussed.

II. THEORY

A. A cylindrical target in free space

The BIEM for a cylinder in free space is first described. First, the problem is considered at a fixed angular frequency ω and we write the three-dimensional Helmholtz Equation, for a rigid scatterer, as

$$p(r, z, \theta) = p^{inc} - \int_{S'} \int_0^{2\pi} \frac{\partial G(r, z, \theta; r', z', \theta')}{\partial n'} p d\theta' dS'. \quad (1)$$

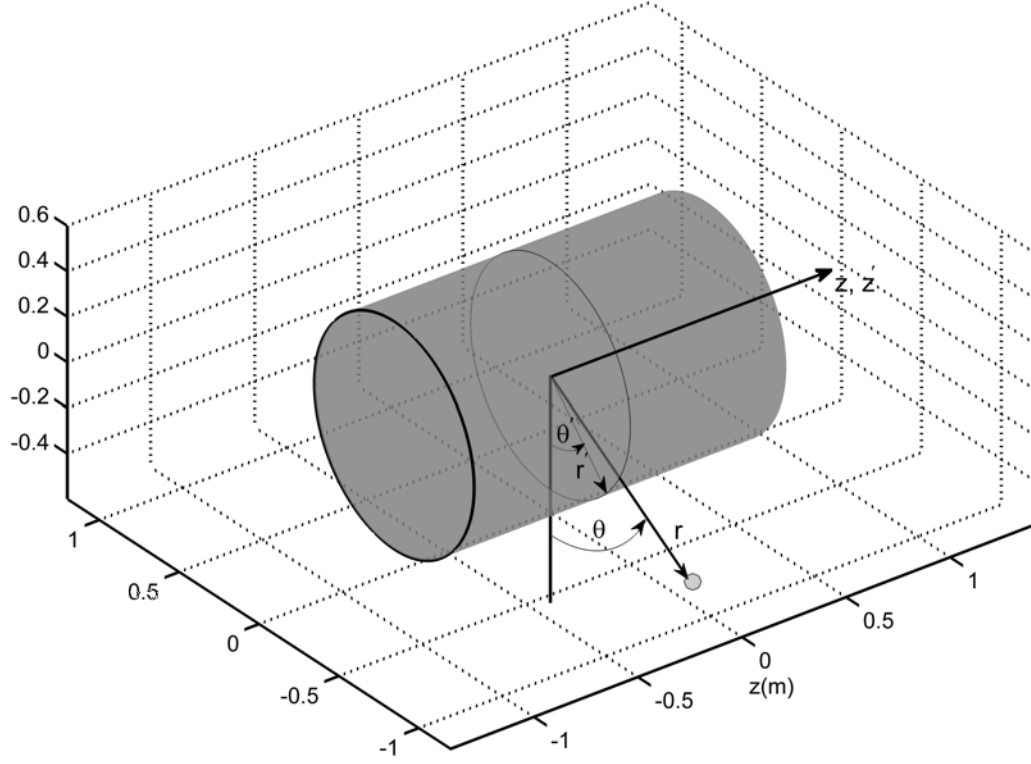


Figure 1: Schematic drawing of a 1.5m long cylinder with radius 0.5. A generic receiver position is shown at $(r, \theta, z = 0)$. A point on the surface at $(r' = 0.5, \theta', z' = 0)$ is also shown.

Here we are taking the normal vector to point out of the cylinder into the surrounding fluid. The coordinates r, r' are the radial coordinates with respect to the cylinder axis and z, z' are the coordinates along the axis of the cylinder. The normal vector will have components in the r' and z' directions of the cylinder. A schematic of a three-dimensional cylinder and its notation is shown in Fig. 1.

The three-dimensional Green's function G is given by

$$G(r, z, \theta; r', z', \theta') = -\frac{\exp(i\omega/c|\vec{R} - \vec{R}'|)}{4\pi|\vec{R} - \vec{R}'|} \quad (2)$$

where c is the speed of sound in the surrounding fluid and \vec{R} denotes the three-dimensional position vector. Let us expand the unknown pressure field on the surface of the target, $p(r, z, \theta)$, as

$$p(r, z, \theta) = \sum_{m=-M}^M p_m(r, z) \exp(im\theta) \quad (3)$$

where the infinite Fourier sum has been truncated.

We write the distance term in the Green's function of Eq.(2) as

$$|\vec{R} - \vec{R}'| = \sqrt{r^2 + (r')^2 - 2rr'\cos(\theta - \theta') + (z - z')^2}. \quad (4)$$

Substituting the Fourier expansion for p , Eq.(3) into Eq.(1), the expression

$$\begin{aligned} p(r, z, \theta) &= p^{inc} + \int_{S'} \int_0^{2\pi} \frac{\partial}{\partial n'} \frac{\exp(i\omega/c\sqrt{r^2 + (r')^2 - 2rr'\cos(\theta - \theta') + (z - z')^2})}{4\pi\sqrt{r^2 + (r')^2 - 2rr'\cos(\theta - \theta') + (z - z')^2}} \\ &\times \sum_{m=-M}^M p_m(r', z') \exp(im\theta') d\theta' r'(S') dS' \end{aligned} \quad (5)$$

is obtained. The (r', z') perimeter of the cylinder is denoted by S' . Performing the azimuthal integral and using the substitution that $\psi \equiv (\theta - \theta')$ one obtains

$$p(r, z, \theta) = p^{inc} + \sum_{m=-M}^M \exp(im\theta) \int_{S'} g_m(r, z; r', z') p_m(r', z') r'(S') dS' \quad (6)$$

where

$$g_m(r, z; r', z') = \int_0^{2\pi} \frac{\partial}{\partial n'} \frac{\exp(i\omega/c\sqrt{r^2 + (r')^2 - 2rr'\cos(\psi) + (z - z')^2})}{4\pi\sqrt{r^2 + (r')^2 - 2rr'\cos(\psi) + (z - z')^2}} \exp(-im\psi) d\psi. \quad (7)$$

Multiplying Eq.(6) by $\exp(-im_1\theta)/(2\pi)$ and integrating with respect to θ over the interval $[0, 2\pi]$, we obtain from the orthogonality of $\exp(-im_1\theta)$

$$p_{m_1}(r, z) = p_{m_1}^{inc}(r, z) + \int_{S'} g_{m_1}(r, z; r'(S'), z'(S')) p_{m_1}(r'(S'), z'(S')) r'(S') dS', \quad (8)$$

where

$$p_{m_1}^{inc}(r, z) = \frac{1}{2\pi} \int_0^{2\pi} \exp(-im_1\theta) p^{inc}(r, z, \theta) d\theta. \quad (9)$$

(it should be noted that, in fact, we will compute both g_{-m_1} and g_{m_1} in Eq.(7) using a cosine transform over $[0, \pi]$). Thus, for each angular order m_1 we have a system of equations to solve,

$$(I/2 - R_{m_1})\vec{p}_{m_1} = \vec{p}_{m_1}^{inc} \quad (10)$$

where $R_{m_1}\vec{p}_{m_1}$ represents a discrete-matrix version of

$$\int_{S'} g_{m_1}(r, z; r'(S'), z'(S')) p_{m_1}(r'(S'), z'(S')) r'(S') dS'. \quad (11)$$

The matrix I in Eq.(10) is the identity matrix and the factor $1/2$ is a result of the standard limit for the Helmholtz equation as the observation point approaches the surface.

In order to discretize the integral of Eq.(11) we discretize the contour S' into discrete panels. We consider p_{m_1} to be constant over a panel and represent the value at the midpoint of the panel. Similarly we use the midpoint value of r' . For g_{m_1} we will consider the midpanel values of (r, z) and (r', z') except for cases where g_{m_1} exhibits singular behaviour and we will perform an analytic integration over the panel.

From Eq.(7), there is a singular behaviour to g_m as $(r', z') \rightarrow (r, z)$. Let us rewrite Eq.(7) as

$$\begin{aligned} g_m(r, z; r', z') &= \int_0^{2\pi} \frac{\partial}{\partial n'} \left\{ \frac{\exp(i\omega/c\sqrt{r^2 + (r')^2 - 2rr'\cos(\psi) + (z - z')^2})}{4\pi\sqrt{r^2 + (r')^2 - 2rr'\cos(\psi) + (z - z')^2}} \exp(im\psi) \right. \\ &\quad \left. - \frac{1}{4\pi\sqrt{r^2 + (r')^2 - 2rr'\cos(\psi) + (z - z')^2}} \right\} d\psi + \frac{G_S(r, z; r', z')}{4\pi} \end{aligned} \quad (12)$$

where

$$G_S(r, z; r', z') \equiv \int_0^{2\pi} \frac{\partial}{\partial n'} \frac{1}{\sqrt{r^2 + (r')^2 - 2rr'\cos(\psi) + (z - z')^2}} d\psi. \quad (13)$$

The integral of Eq.(13) can be expressed analytically¹¹. In particular, following the notation of Ref. 11,

$$\begin{aligned} G_S(r, z, ; r', z') &= 2n_{r'} \frac{\{R_e^2[E(\kappa) - K(\kappa)(1 - \kappa^2)] - 2r'(r' + r)E(\kappa)\}}{r'R_e^3(1 - \kappa^2)} \\ &- n_{z'} \frac{4(z' - z)E(\kappa)}{R_e^3(1 - \kappa^2)} \end{aligned} \quad (14)$$

where $n_{r'}$ and $n_{z'}$ are the 2 normal components along the cylinder profile and K and E are the complete elliptic integrals of the first and second kinds respectively. The terms R_e and κ are defined by

$$\kappa^2 = \frac{4r'r}{R_e^2}, \quad R_e^2 = (r + r')^2 + (z - z')^2. \quad (15)$$

The first term in Eq.(14) is singular as $r \rightarrow r'$, $z \rightarrow z'$, and $\kappa \rightarrow 1$. However, this term can be analytically integrated over the panel where $\kappa = 1$ by using an expansion of $K(\kappa)$ in the neighbourhood of $\kappa = 1$.

In the case of a flat-ended cylinder, there is another source of singular-like terms which occur in the matrix kernel for points near the edges of the flat endcaps. Consider, for example, the second term in Eq.(14) for (r', z') on the flat endcap and (r, z) along the length of the cylinder. On the endcap $n_{z'} = 1$, but since z is along the length of the cylinder, $z' - z = \Delta z$ is non-zero with the denominator approaching zero as $(r', z') \rightarrow (r, z)$. For these cases, (we will consider the discrete value of $r' = r_j$) one can subtract a term with the correct singular behaviour and add back in a corresponding analytical integral,

$$\begin{aligned} &\int_{r_j - \delta_r/2}^{r_j + \delta_r/2} n_{z'} \frac{4(z' - z)E(\kappa)}{R_e^3(1 - \kappa^2)} dr' \\ &= \int_{r_j - \delta_r/2}^{r_j + \delta_r/2} n_{z'} \left(\frac{4(z' - z)E(\kappa)}{R_e^3(1 - \kappa^2)} - \frac{4(z' - z)}{R_{e,j}((r - r')^2 + (z - z')^2)} \right) dr' \\ &+ 4n_{z'} \text{sgn}(z' - z) \left(\text{Atan}\left(\frac{r - r_j + \delta_r/2}{|z - z'|}\right) - \text{Atan}\left(\frac{r - r_j - \delta_r/2}{|z - z'|}\right) \right) \end{aligned} \quad (16)$$

Similarly, the $n_{r'}$ term in Eq.(14) gives rise to an almost singular term when (r', z') is on the length of the cylinder and (r, z) is on an endcap. In order to deal with these behaviours near the endcaps, simple expressions which capture the singular behaviours are subtracted from all the terms of Eq.(14) and then analytical integrals of these terms are added back in.

The BIEM approach of this paper suffers from the problem of irregular frequencies^{7,8,12}; that is, specific frequencies where the BIEM system of equations does not have a unique solution. In the free space case, these frequencies correspond to the integral equation (the continuous version of Eq.(10)) having a zero eigenvalue. This, in turn, corresponds to a zero eigenvalue for the Dirichlet problem (i.e. $p = 0$ on the boundaries)¹² for the interior of the target. For the flat-ended cylinder, these irregular frequencies can be analytically predicted. The interior Dirichlet problem, for azimuthal order m , is solved by eigenfunctions of the form

$$\Psi(r, z) = \sin(n\pi/Lz)J_m((\sqrt{\omega^2/c^2 - (n\pi/L)^2}r). \quad (17)$$

Denoting the radius of the cylinder as r_0 , then for a given azimuthal order, the irregular frequencies are given by

$$f_{n,q} = \frac{c}{2\pi} \sqrt{(\frac{n\pi}{L})^2 + (\frac{\tau_q}{r_0})^2}. \quad n = 1, \dots, \infty, q = 1, \dots, \infty \quad (18)$$

(see, also, Ref. 12) where τ_q is a zero of $J_m(u)$. In this paper, we will add N_{sh} extra interior points at which to evaluate the Helmholtz equation. As these field points are in the interior of the cylindrical object, the interior Helmholtz equation applies. For example, for the set of interior points at (r_q, z_q) , the interior equation is:

$$p_m^{inc}(r_q, z_q) = - \sum_{j=1}^N R_m(r_q, z_q; r_j, z_j) p(j) \quad (19)$$

where R_m is the discrete kernel at angular order m . In our implementation, the N_{sh} points are displaced along radials connecting the interior origin of the cylinder to its

(r', z') perimeter. The distance to be displaced along the radials is an user input. For each radial, this distance is varied by a small random amount. For each angular order, m , we will have a $(N + N_{sh}) \times N$ system of equations to solve in a least-squares sense. As was shown in Ref.12, the resulting system of equations now has an unique solution.

B. A cylinder below an interface

The previous derivation of the BIEM considered an axi-symmetric target in free space. In the case that the target is below a pressure-release interface, the appropriate three-dimensional Green's function is

$$G(R; R') = -\frac{\exp(i\omega/c|\vec{R} - \vec{R}'|)}{4\pi|\vec{R} - \vec{R}'|} + \frac{\exp(i\omega/c|\vec{R} - \tilde{\vec{R}}'|)}{4\pi|\vec{R} - \tilde{\vec{R}}'|} \quad (20)$$

where $\tilde{\vec{R}}'$ denotes the position vector of the image point of \vec{R}' .

This expression can be used in Eq.(1) . Once again, the unknown pressure field on the surface of the cylindrical object can be expanded in a Fourier series with unknown coefficients. However, in general, the sets of equations for the various azimuthal orders are coupled, unlike the free space case where the integral equations for the different azimuthal orders were uncoupled. The one exception occurs when the cylinder is oriented vertically so that the vertical axis is the axis of symmetry for the scattering problem. In this case, the systems of equations for the various azimuthal orders remain uncoupled.

Instead of using the full three-dimensional Green's function of Eq.(20) in Eq.(1) to account for the presence of the interface, let us consider an iterative solution to the problem using the free-space Green's function. The zero'th order solution \vec{s}_0 will be determined by considering the incident field from a point source and its negative image with respect to the upper interface. However, the solution on the surface of the cylinder will be computed by using only the free-space Green's function in the

integral equation. The azimuthally uncoupled approach can be used in this case. This solution can then be propagated back to a receiver using the half-space Green's function. Thus, the upper interface is accounted for with respect to the incident and scattered fields, but not in the solution of the integral equation itself. This corresponds to the single-scattering solution as discussed by various authors^{2,6}.

In reality, the field scattered from the target reflects from the upper interface and is reincident upon the target. This rescattering process will be characterized by an azimuthal conversion matrix $C_{nm}(\vec{R}_i, \vec{R}_j)$. This matrix expresses the n th azimuthal coefficient of the pressure field reincident upon the cylinder at a discrete point \vec{R}_i due to a solution coefficient of unity for the m th azimuthal order at the discrete point \vec{R}_j . Considering all the possible azimuthal orders (positive and negative as well) and all the discretization points of the cylinder, there is a global conversion matrix C of dimension $(2M+1)(N+N_{sh}) \times (2M+1)N$ where M is the number of azimuthal orders, N is the number of discretization points and N_{sh} is the number of added interior points for Schenke's method. Let us denote the zero-th order solution upon the target as \vec{s}_0 . Then the series or iterative solutions can be formally expressed as

$$\begin{aligned} \vec{s} &= \vec{s}_0 + (G_0)^{-1}C\vec{s}_0 + (G_0)^{-1}C(G_0)^{-1}C\vec{s}_0 + \dots((G_0)^{-1}C)^N\vec{s}_0 + \dots \\ &= (I - (G_0)^{-1}C)^{-1}\vec{s}_0 = (G_0 - C)^{-1}G_0\vec{s}_0 = (G_0 - C)^{-1}p^{inc}. \end{aligned} \quad (21)$$

The concept of irregular frequencies, and their relationship to the eigenvalues of the interior Dirichlet problem was discussed for the case of a target in free space. In the case of a target below an interface, the irregular frequencies for the exact BIEM formulation are the same as for the free space case. In order to prove this, the theorems of Ref. 12 (text and appendix) are followed. However, instead of considering the free space Green's function (or its normal derivative) as the kernel in these theorems, one can use the half-space Green's function (with the target considered in the half-space domain) without changing the approach of Ref.12.

C. Computation of the conversion matrix C

We now consider the computation of the conversion matrix C , either to use in the iterative approach or in the exact matrix $(G_0 - C)$ of Eq.(21). Given a pressure distribution upon the object, what is the resulting field reincident upon the object due to the scattered field? We found it helpful in our derivation to replace the original half-space problem with the equivalent infinite space problem, where there is negative image source reflected above the interface and also a reflected image of the target shape. In the following, we refer to the target in the water as the real cylinder and the reflected target as the image cylinder. There is a local (r, z, θ) coordinate system for each of the cylinders where θ on the image cylinder has the same orientation as on the real cylinder. These coordinate systems are illustrated in Fig. 2. Due to the mirror-symmetry of the problem, if the pressure field on the real cylinder is denoted as p_R , then the pressure field p_I on the image cylinder is given by

$$p_I(r'_i, z'_i, \theta'_i) = -p_R(r'_i, z'_i, \pi - \theta'_i) \quad (22)$$

where for p_R the coordinates on the real cylinder are the mirror-image coordinates of those on the image cylinder. In terms of the Fourier coefficients c_m of the pressure field on the real cylinder,

$$p_I(r_p, z_p) = \sum_{m=-M}^M -c_{-m}(r_p, z_p) \exp(im\theta_i) \exp(im\pi). \quad (23)$$

Now, let us consider the field incident upon the real cylinder due to a pressure field of the form of Eq.(23) on the image cylinder. The three-dimensional free-space Green's function is used to propagate the field from the image cylinder back to the real cylinder,

$$p_R = p(r_i, z_i, \theta_i) = - \int_{S'} \int_0^{2\pi} \frac{\partial G(r_i, z_i, \theta_i; r'_i, z'_i, \theta'_i)}{\partial n'} p_I d\theta'_i dS'_i \quad (24)$$

where all the coordinates refer to the coordinate system of the image cylinder. For the representation of the Green's function, the following Fourier-Bessel expansion is

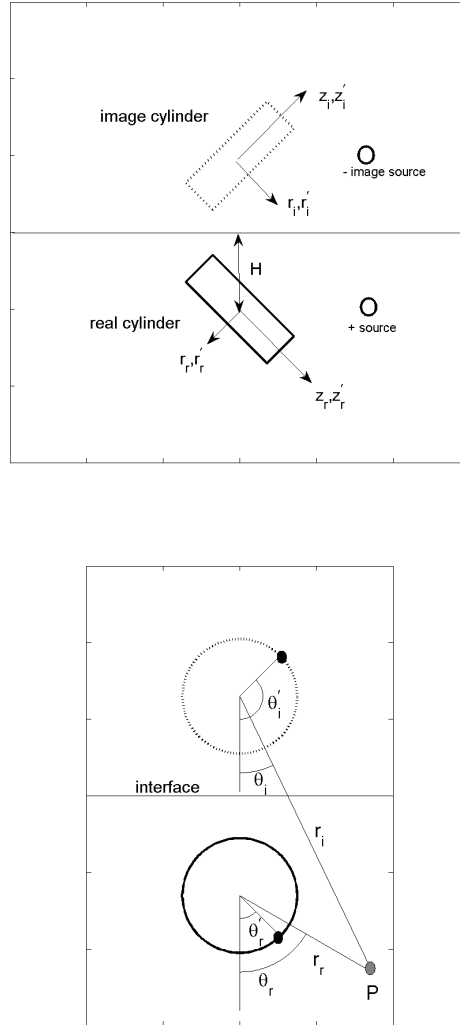


Figure 2: Schematic drawings of geometry and notation for (upper) tilted cylinder with a source and the mirror image. The tilted cylinder has a centre offset H . (lower) The angular coordinate system is shown on the endcaps of a cylinder lying parallel to the interface. A receiver point P is indicated with the angles θ_r and θ_i the azimuthal angles measured from the lower and image cylinders, respectively.

used,

$$G(r_i, z_i, \theta_i; r'_i, z'_i, \theta'_i) = \frac{1}{2\pi} \sum_{m=-M}^M \left(\int_{-\infty}^{\infty} \exp(ik_z(z_i - z'_i)) J_m(\gamma r'_i) H_m(\gamma r_i) / (4i) dk_z \right) \exp(im(\theta_i - \theta'_i)). \quad (25)$$

(this form can be simply derived by taking the azimuthal and z-Fourier transforms first and then constructing the radial Green's function for azimuthal order m). For the case of a finite cylinder with constant radius r_0 , then the normal derivative of the Green's function corresponds to either the r'_i derivative along the length of the cylinder and the z'_i derivative at the end caps. Utilizing Eqs.(23)-(25), and performing the azimuthal integration in Eq.(24), the resulting expression for the field reincident upon the real cylinder due to the solution coefficient c_m is

$$\begin{aligned} p_m(r_i, z_i, \theta_i) &= - \left(\int_{-L}^L c_m(r'_i = r_0, z'_i) \left(\int_{-\infty}^{\infty} \exp(ik_z(z_i - z'_i)) \frac{d}{dr'_i} J_{-m}(\gamma r'_i) \right. \right. \\ &\quad \times \left. \left. H_{-m}(\gamma r_i) dk_z \right) r_0 dz'_i \right) \times \exp(-im\theta_i) \exp(-im\pi) / (4i) \\ &\quad + \text{endcap contributions} \end{aligned} \quad (26)$$

In the following, we will concentrate upon the expressions for the reincident field due to the pressure field along the length of the image cylinder. The expressions for the endcap contributions are similar, but involve the z-derivative of the Green's function. For example, the expression for the contribution from the endcap ($Z = L$) with the normal in the positive z direction is given by

$$\begin{aligned} p_{m,ec} &= - \int_0^{r_0} c_m(r' = r_0, z') \left(\int_{-\infty}^{\infty} -ik_z \exp(ik_z(z_i - L)) J_{-m}(\gamma r'_i) H_{-m}(\gamma r_i) dk_z \right) r_i dr'_i \\ &\quad \times \exp(-im\theta_i) \exp(-im\pi) / (4i). \end{aligned} \quad (27)$$

In order to utilize Eqs.(26) and (27) for real cylinder coordinates, they will need to be converted into the image cylinder coordinates. One of the discretization points

(r^q, z^q) along the real cylinder is considered. For the value of r_q , the Cartesian values as a function of an angular variable are considered

$$x_q(\theta) = r_q \cos \theta, y_q(\theta) = r_q \sin \theta \quad (28)$$

The Cartesian points $(x_q(\theta), y_q(\theta), z_q)$ are then converted into the coordinate system of the image cylinder to yield the new coordinates $z_i(z_q, x_q(\theta)), r_i(z_q, x_q(\theta), y_q(\theta)), \theta_i(z_q, x_q(\theta), y_q(\theta))$. We now consider a discrete version of Eq.(26) for one of the the BIEM discretization points, $z'_i = z_p, r'_i = r_p$. The conversion matrix for the (n, m) element is computed by projecting $\exp(-in\theta)$ upon the expressions from Eqs.(26) and (27) ,

$$C_{nm}(r_q, z_q; r_p, z_p) = -\frac{1}{2\pi} \int_0^{2\pi} \int_{-\infty}^{\infty} \exp(-in\theta) \exp(-im\theta_i(z_q, x_q(\theta), y_q(\theta))) \quad (29)$$

$$\times \exp(ik_z(z_i(z_q, x_q(\theta)) - z_p)) \frac{d}{dr} J_{-m}(\gamma r_p) H_{-m}(\gamma r_i(z_q, x_q(\theta), y_q(\theta))) \exp(im\pi) \frac{r_0 \Delta_p}{4i} d\theta dk_z.$$

where Δ_p is the discrete length of the p th BIEM panel. In this equation the term $c_m(r'_i = r_0, z'_i)$ of Eq.(26) is replaced by the value unity as we are considering the conversion matrix.

The azimuthal integral of Eq.(29) is performed by utilizing a numerical discretization. The expression of Eq.(29) is for (r_p, z_p) on the length of the cylinder. There is a similar expression for (r_p, z_p) on the endcaps. Numerically, all the (p, q) sets of points are considered one-by-one and the coefficients for all values of the input and output azimuthal orders (n, m) computed. The expression of Eq.(29) is not always valid as it is assumed in the derivation that $r_i \geq r_p$. For example, if the cylinder is oriented vertically there are values of r_i on the endcaps and values of r_p on the image cylinder such that $r_i < r_p$ and this representation breaks down. There are, however, alternate valid representations which can be used in this case.

In the case that the real cylinder is lying parallel to the interface, the mathematics can be simplified using the addition theorem¹³ for cylindrical Bessel Functions. In particular, in Eq.(26), the term

$$H_{-m}(\gamma r_i) \exp(-im\theta_i) = \exp(-im\pi) \sum_{n=-\infty}^{\infty} J_n(\gamma r) H_{n+m}(\gamma D) \exp(in\theta) \exp(in\pi) \quad (30)$$

where r, θ refer to coordinates measured from the axis of the real cylinder and D is twice the distance from the interface (H in Fig. 2).

In this case, one obtains

$$\begin{aligned} C_{nm}(r_q, z_q; r_p, z_p) &= -\exp(in\pi)/(4i)r_p\Delta_p \\ &\times \int_{-\infty}^{\infty} \exp(ik_z(z_q - z_p)) \frac{d}{dr} J_m(\gamma r_p) J_n(\gamma r_q) H_{n-m}(\gamma D) dk_z \end{aligned} \quad (31)$$

This result is for (r_p, z_p) along the length of the cylinder. The result for a discrete panel in one of the endcaps is similar,

$$\begin{aligned} C_{nm}(r_q, z_q; r_p, z_p) &= -\exp(in\pi)/(4i)r_p\Delta_p \\ &\times \int_{-\infty}^{\infty} -ik_z\alpha_z \exp(ik_z(z_q - z_p)) J_m(\gamma r_p) J_n(\gamma r_q) H_{n-m}(\gamma D) dk_z \end{aligned} \quad (32)$$

where $\alpha_z = 1$ for the upper endcap and $\alpha_z = -1$ for the lower endcap. These integrals would appear to involve a fair amount of computation. However, the computations can be made very vectorizable. The k_z integral is truncated and discretized for a set of $(k_{z,j}, j = 1, \dots, N_z)$. A $N_I \times N_z$ matrix is computed for N_I the number of discrete panels for the BIEM. A matrix can be defined for the points along the image cylinder,

$$\begin{aligned} C_S(p, k_{z,j}) &= -\exp(in\pi)c_m(r_p, z_p)\Delta_p\Delta_{k_{z,j}} \\ &\times r_p f_p(\gamma_j r_p) \exp(-ik_{z,j}z_p) H_{n-m}(\gamma_j D) \frac{dJ_m(\gamma_j r_p)}{dr} \end{aligned} \quad (33)$$

and a matrix for points along the real cylinder,

$$C_R(q, k_{z,j}) = \exp(ik_{z,j}z_q) J_n(\gamma_j r_p)/(4i). \quad (34)$$

Here $k_{z,j}$ is a discrete value of k_z , $\Delta_{k_{z,j}}$ is the corresponding differential (computationally, we will add a small imaginary component to k_z and thus the differential is complex and in our implementation varies with respect to the real value of k_z). Then Eq.(32) can be written compactly as

$$C_{nm}(r_q, z_q; r_p, z_p) = C_R(q, k_{z,j})C_S^T(p, k_{z,j}) \quad (35)$$

It can be seen that for different azimuthal orders (n, m) , $C_R(n)$ and $C_S(m)$ are not coupled with respect to the azimuthal orders with the exception of the term $H_{n-m}(\gamma_j D)$.

III. NUMERICAL EXAMPLES

As a benchmark case, a rigid sphere beneath the interface is considered. In this case, the most straightforward approach to solving the problem is to consider the axis of symmetry as being the vertical axis. Even with the upper interface, the problem is still axi-symmetric and one can use a de-coupled Fourier approach. There are a variety of approaches for solving this problem. In this paper, we use the method of virtual sources or wavefield superposition⁹⁻¹¹. A set of 301 point sources of the form

$$S_1(r, z, \theta : r', z', \theta') = -\frac{1}{4\pi} \left(\frac{\exp(ikR_1)}{R_1} - \frac{\exp(ikR_2)}{R_2} \right) \quad (36)$$

is used, where

$$\begin{aligned} R_1 &= \sqrt{r^2 + (r')^2 - 2rr' \cos \psi + (z - z')^2} \\ R_2 &= \sqrt{r^2 + (r')^2 - 2rr' \cos \psi + (z + z')^2} \end{aligned} \quad (37)$$

and $\psi = \theta - \theta'$. The second term in Eq.(37) accounts for the upper interface. The coordinates for a set of point sources (r', z') are displaced radially inwards from the surface of the sphere by $\delta_1 = 0.007$ m. The point sources for the m th azimuthal order are computed from the three-dimensional point sources,

$$s_{m,1} = \int_0^\pi S_1(r, z; r', z'; \psi) \cos m\psi d\psi \quad (38)$$

As with the standard BIEM, the method of wavefield superposition suffers from irregular frequencies¹⁰. As a remedy to this, we consider another set of point sources, $s_{m,2}$ displaced inwards from the sphere's surface by $\delta_2 = 0.0072$ m. Then we consider the composite Green's functions of the form

$$s_m = (1 + 1000i/k)s_{m,1} + (1 - 1000i/k)s_{m,2}. \quad (39)$$

This form of Green's function has both monopole and dipole contributions. For each angular order m we solve a system of equations of the form,

$$\frac{\partial s_m(r_i, z_i, r'_j, z'_j)}{\partial n} \vec{a}_m = \frac{\partial p_m^{inc}(r_i, z_i)}{\partial n}, \quad i = 1, \dots, N, j = 1, \dots, N \quad (40)$$

where \vec{a}_m is the vector of unknown coefficients and $N = 301$ in our case. Once these coefficients have been determined, then the pressure field at a receiver location can be constructed by a Fourier superposition of the fields computed at the receiver for each azimuthal order.

In the first example, a rigid sphere of radius 0.4 m is located 1 m below the upper scattering surface. We use both the superposition and the cylindrical BIEM (but for a sphere) methods to compute the scattered pressure field as a function of frequency for source/receiver pairs located at a range of 10m from the sphere centre (below the sphere) and at angles of 0,30, and 60 degrees off the vertical axis (axis is oriented downwards). We will compute the full-scattering solutions. For the virtual source technique we used 301 sources at all frequencies - the number of azimuthal orders was computed from the formula $N_\theta = \text{round}(1.5\omega \times 0.4/1500. + 6)$. For the cylindrical BIEM approach, we used 201 discretization points along the surface and 17 additional interior points for Schenck's method. The number of azimuthal orders was computed from $N_\theta = \text{round}(1.5\omega \times 0.4/1500. + 5)$ (or, in general, for the value of 0.4 we use the radius of the cylinder). It should be emphasized that for the cylindrical BIEM, the axis of symmetry of the sphere is taken to be the horizontal axis and the

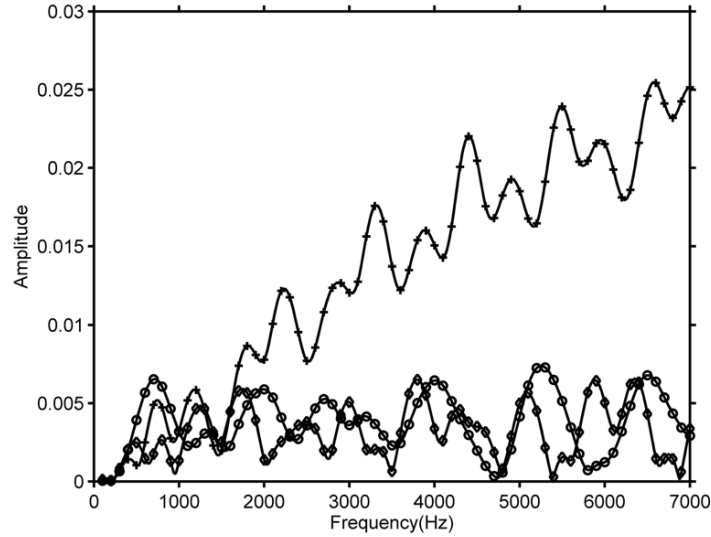


Figure 3: A comparison of the computed backscattered spectra using the virtual source technique (solid lines) and the cylindrical BIEM (markers) for source/receiver 60° (circles), 30° (diamonds), and 0° (+) off the vertical axis below the sphere. For clarity, the symbols are shown at every fifth frequency value.

azimuthal problem is fully coupled. In Fig. 3, the spectra of the scattered fields as computed using the virtual source (solid) and the cylinder BIEM method (markers) are shown for the angles of 0, 30, and 60 degrees (0° corresponds to normal incidence from below). As can be seen the agreement between the 2 methods is excellent.

Having obtained excellent agreement of our cylindrical method with a virtual source approach for a sphere near an interface, the case of a flat-ended cylinder is considered. The cylinder is discretized with 301 points and 21 interior points are used for Schenck's method. It has a total length of 1.5 m, a radius of 0.25 m and its centre is located 1 m below the water/air interface. For the cylinder, there will be a combination of specular reflections from the length of the cylinder, endcap reflections, and diffractions from the edges of the endcaps. In Fig. 4, we show the computed spectra for the 3 angles of source/receivers (the same angles as for the sphere) for all

interactions (solid) and the single scatter solution (markers). As with the sphere, the spectra for the 60° incidence are very similar, for 30° there are observable differences, and for normal incidence the differences are large.

It is interesting to consider the solution of the BIEM without using the additional interior points for Schenke's method. From Eq.(18), the values of the irregular frequencies can be predicted for the case of flat-ended cylinder. In Fig. 5a, we show the computed spectra (a 5 Hz spacing is used) for the 3 source/receiver angles used in the previous example. Both the azimuthally-uncoupled solution (single-scatter, dashed) and the fully coupled solution (solid) are shown. However, no additional interior points are used in the computations. As can be seen there are frequencies near which the spectral amplitude is poorly behaved as a function of frequency. This behaviour is more noticeable for some source/receiver angles. This is likely due to the differing projections of the solution onto the eigenfunction corresponding to this frequency. The frequency values predicted by Eq.(18) are shown in Fig. 5a as vertical lines. In Fig. 5b, the computed Condition Number (ratio of amplitude of largest to smallest eigenvalue for a matrix using the MATLAB routine) for the fully coupled matrix(solid) and uncoupled matrix (dashed, single-scatter approximation) are shown. The condition number behaviour is so similar for the coupled and uncoupled matrices that is difficult to distinguish the different lines in Fig. 5b. Once again, for the full and single-scatter method, the poor solution behaviour is related to the proximity of irregular frequencies and as discussed earlier, these values are the same for the fully coupled and uncoupled matrices.

Finally, we consider the case of the cylinder tilted at -45° (see Fig. 2) with respect to the vertical. Three different source/receiver positions are considered, 10 m range and at 45° , 60° , and 90° off the vertical (and to the right of the tilted cylinder in Fig. 2). For the source/receiver at 45° there is a specular reflection off the endcap of the cylinder. For the source/receiver at 60° off vertical, there is a ray which reflects off

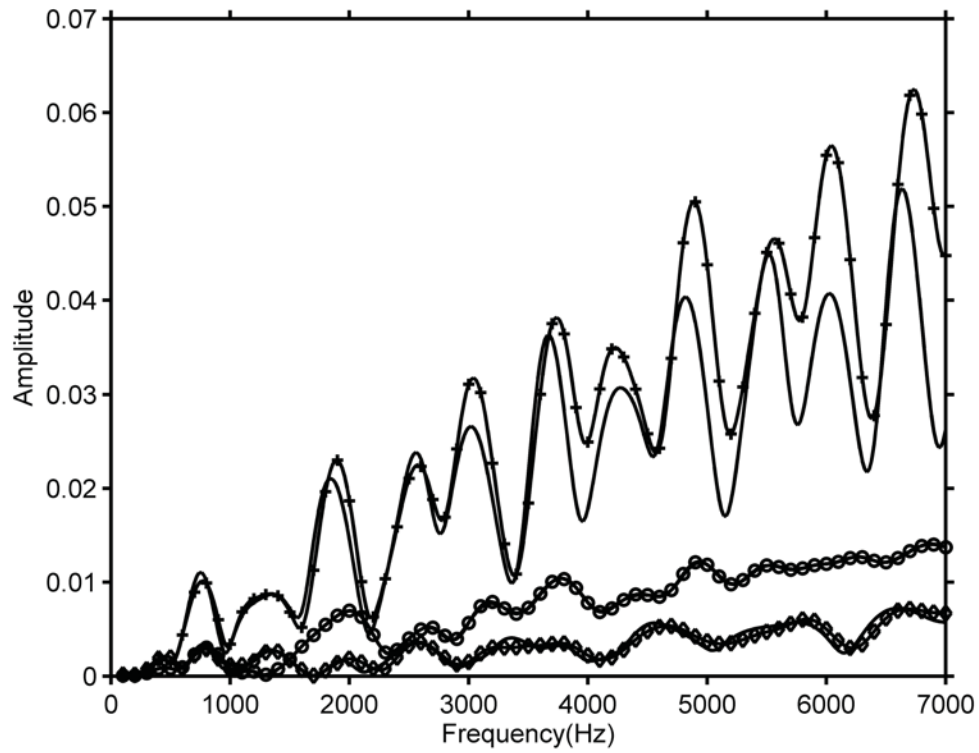


Figure 4: A comparison of the computed backscattered spectra using the cylindrical BIEM with the full solution (solid lines) and the single-scatter solution (lines with markers) for source/receiver 60° (circles), 30° (diamonds), and 0° (+) off the vertical axis below the cylinder. For clarity, the symbols are shown at every fifth frequency value.

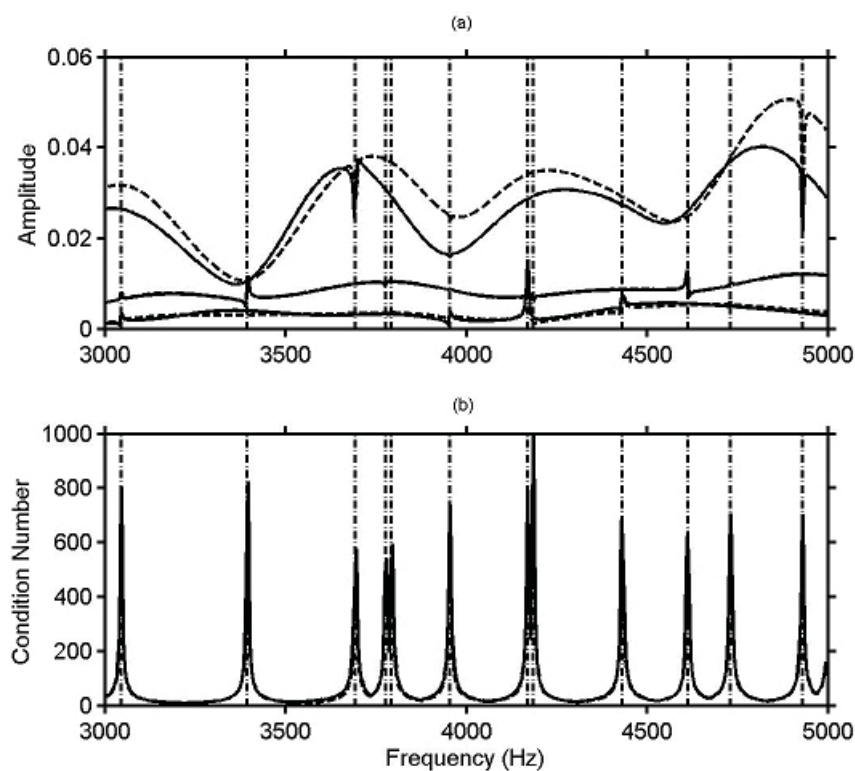


Figure 5: (a) The computed backscattered spectral amplitude for the source/receiver configurations of Fig. 4 using full solution (solid) and single-scatter solutions (dashed). There have been no additional interior points used in the computations. (b) The computed matrix condition number for the full solution matrix (solid) and uncoupled single-scatter matrix (dashed). For both plots, the vertical lines indicate the predicted locations of the eigenfrequencies of the interior Dirichlet problem.

the upper surface and is then incident upon the cylinder at close to broadside. This energy is then reflected back off the top surface before returning to the receiver. This is still a single-scattering event as there is only one reflection off the cylinder. Finally, for the source/receiver along the horizontal (90°), the tilted cylinder is a type of corner reflector. A horizontal ray is reflected vertically upwards and then is reflected by the upper surface downwards and is then converted back to a horizontal ray after a second reflection from the cylinder. In Fig. 6 we show the computed spectra with all interactions (solid line) and with the single scatter approximation (markers). The circles correspond to the 45° source/receiver, the diamonds the 60° case, and the plus signs, the horizontal source/receiver. The largest differences between the single-scatter (line with + markers at the bottom of the figure) and the full-scattering solution (unassociated line near the middle of the figure) occur for the horizontal source/receiver. This large difference is anticipated from the previous discussion with respect to the strong echo from 2 interactions with the cylinder. In Fig. 7 we show the computed echo time series for an incident 2500 Hz Ricker wavelet. The large multiple-scattering echo can be seen in Fig. 7c as predicted by simple ray considerations (solid lines, full solution, dashed lines, single-scatter solutions).

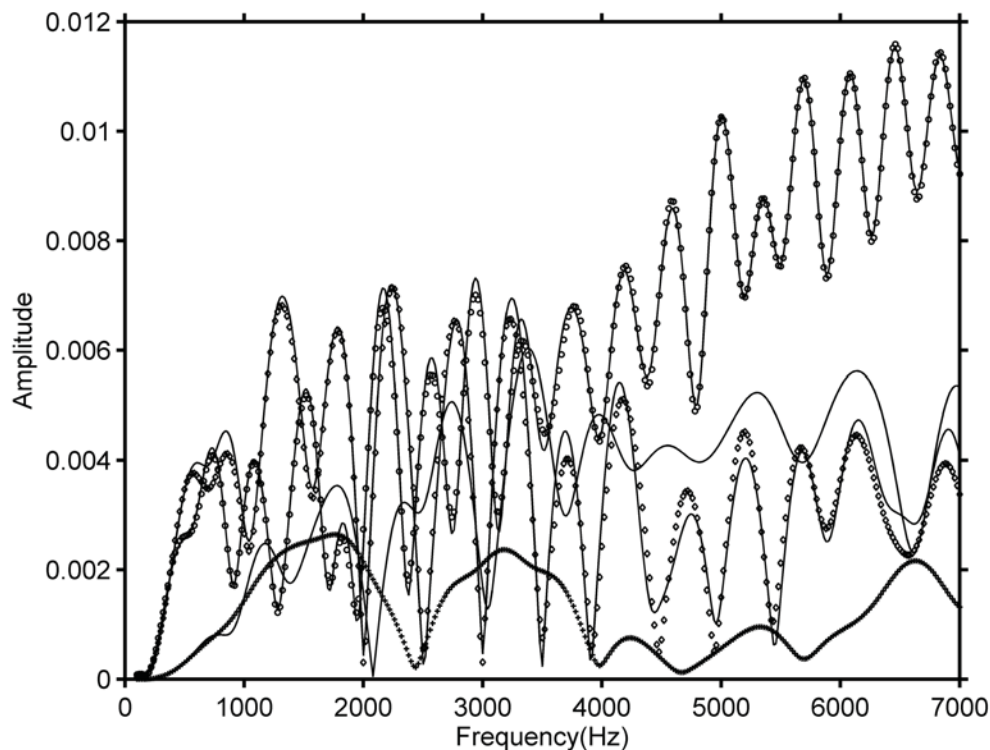


Figure 6: A comparison of the computed backscattered spectra using the cylindrical BIEM with the full solution (solid lines) and the single-scatter solution (markers) for source/receiver 45° (circles), 60° (diamonds), and 90° (+) off the vertical axis below the cylinder. The cylinder is tilted at -45° with respect to the horizontal. For clarity, the symbols are shown at every fifth frequency value. The full-scattering solution for 90° is the line near the vertical centre of the plot which appears unassociated.

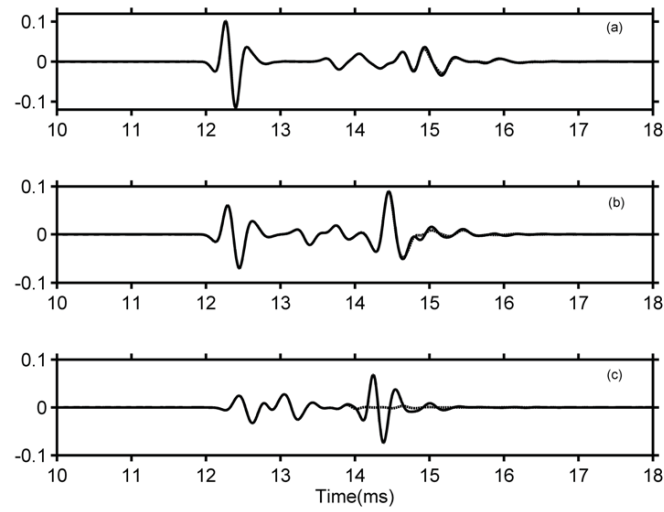


Figure 7: The computed echo time series for a 2500-Hz Ricker wavelet using the full solution (solid line) and the single-scatter solution (dashed) for: (a) 45° off the vertical, (b) 60° off the vertical and (c) 90° off the vertical.

IV. DISCUSSION OF RESULTS

In this paper a modified azimuthally-symmetric BIEM was presented for the solution of scattering from cylindrical objects below a pressure-release interface. Although the results shown are for a sphere and a flat end-capped cylinder, the methods described are valid for more general target shapes with azimuthal symmetry. The scattering process for the cylindrical object in free space can be constructed by solving a sequence of two-dimensional problems, one for each angular order. When the interactions between the object and the interface are considered then there is coupling between the Fourier orders. The computation of this azimuthal conversion matrix is described for the cases of the cylinder lying parallel to the interface and also for the cylinder tilted with respect to the interface. For the case of the parallel cylinder, this conversion matrix can be efficiently computed by using a wavenumber integral. When the conversion matrix is set to zero, the resulting computed pressure field corresponds to the single-scattering approximation.

In the numerical examples, the proposed method was first benchmarked against another solution method for a sphere and the agreement was found to be excellent. Different scattering geometries were considered for a cylinder parallel to the interface and for a cylinder tilted at -45° with respect to the vertical. For the parallel cylinder it was found that for small monostatic scattering angles with respect to the cylinder's axis, the single-scattering solution was accurate and became less accurate as the scattering angle increased. For the tilted cylinder, the cylinder and the interface combined to form a corner-like reflector and in this case there was a strong, multiple-scattering return for the source/receiver parallel to the interface. The significant difference with the single-scattering solution was evident in both the spectral and time domains.

In the method of this paper, the problem of irregular frequencies was addressed by using additional interior equations in the BIEM. In order to investigate the location

of the irregular frequencies for the single-scatter (uncoupled) and fully-coupled approaches the extra interior equations were removed. The computational values of the irregular frequencies appeared to be in excellent agreement with the theoretically predicted values and these values were the same for the single-scatter and fully-coupled formulations.

References

- [1] R.H. Hackman and G.S. Sammelmann, “Multiple-scattering analysis for a target in an oceanic waveguide”, J. Acoust. Soc. Am., Vol.84, pp. 1813-1825, 1988.
- [2] J.A. Fawcett, W.L.J. Fox, and A. Maguer, “Modeling of scattering by objects on the seabed”, J. Acoust. Soc. Am., Vol. 104, pp.3296-3304 (1998).
- [3] R. Lim, J.L. Lopes, R.H. Hackman, and D.G. Todoroff, “Scattering by objects buried in underwater sediments: Theory and experiment”, J. Acoust. Soc. Am., **93**, pp. 1762–1783, 1993.
- [4] M. Zampolli, A. Tesei, F.B. Jensen, N. Malm, and J.B. Blottman, III, “A computationally efficient finite element model with perfectly matched layers applied to scattering from axially symmetric objects.”, J. Acoust. Soc. AM. **122**, pp. 1472–1485, 2007.
- [5] K.L. Williams, S.G. Kargl, E. Thorsos, D. Burnett, J. Lopes, m. Zampolli, and P. Marston, “Acoustic scattering from a solid aluminum cylinder in contact with a sand sediment: Measurements, modeling, and interpretation”, J. Acoust. Soc. AM. **127**, pp. 3356–3371, 2010.
- [6] J. Sessarego, P. Cristini, N. Grigorieva, and G. Fridman, “Measurements and modeling of acoustic scattering by a spherical elastic shell near an interface”, in *Proceedings of Fourth International Conference and Exhibition: Underwater Acoustic Measurements: Technologies and Results*, Kos, Greece, 20-24 June 2011, pp.801-808.
- [7] A.F. Seybert, B. Soenarko, F.J. Rizzo, and D.J. Shippy, “A special integral equation formulation for acoustic radiation and scattering for axisymmetric bodies and boundary conditions”, J. Acoust. Soc. Am., **80**, pp.1241–1247, 1986.

- [8] J. J. Grannell, J.J. Shirron, and L.S. Couchman, “A hierarchic p-version boundary-element method for axisymmetric acoustic scattering and radiation”, J. Acoust. Soc.Am., **95**, pp. 2320-2329, 1994.
- [9] I. Lucifredi and H. Schmidt, “Subcritical scattering from buried elastic shells”, J. Acoust. Soc. Am., **120**, pp. 3566–3583, 2006.
- [10] D.T. Wilton, I.C. Mathews, and R.A. Jeans, “A clarification of nonexistence problems with the superposition method”, J. Acoust. Soc. Am., **94**, pp. 1676–1680, 1993.
- [11] G. Fairweather, A. Karageorghis, and P.A. Martin, “The method of fundamental solutions for scattering and radiation problems”, Engineering analysis with boundary elements, **27**, pp. 759–769, 2003.
- [12] H.A. Schenck, “Improved integral formulation for acoustic radiation problems”, J. Acoust. Soc. Am., **44**, pp. 41-58, 1968.
- [13] I.S. Gadshteyn and I.M. Ryzhik, *Table of Integrals, series, and Products*, Academic Press, NewYork, 1965, p.979.

List of Figures

Figure 1 - Schematic drawing of a 1.5m long cylinder with radius 0.5. A generic receiver position is shown at $(r, \theta, z = 0)$. A point on the surface at $(r' = 0.5, \theta', z' = 0)$ is also shown.

Figure 2 - Schematic drawings of geometry and notation for (upper) tilted cylinder with a source and the mirror image. The tilted cylinder has a centre offset H . (lower) The angular coordinate system is shown on the endcaps of a cylinder lying parallel to the interface. A receiver point P is indicated with the angles θ_r and θ_i the azimuthal angles measured from the lower and image cylinders, respectively.

Figure 3 - A comparison of the computed backscattered spectra using the virtual source technique (solid lines) and the cylindrical BIEM (markers) for source/receiver 60° (circles), 30° (diamonds), and 0° (+) off the vertical axis below the sphere. For clarity, the symbols are shown at every fifth frequency value.

Figure 4 - A comparison of the computed backscattered spectra using the cylindrical BIEM with the full solution (solid lines) and the single-scatter solution (lines with markers) for source/receiver 60° (circles), 30° (diamonds), and 0° (+) off the vertical axis below the cylinder. For clarity, the symbols are shown at every fifth frequency value.

Figure 5 - (a) The computed backscattered spectral amplitude for the source/receiver configurations of Fig. 4 using full solution (solid) and single-scatter solutions (dashed). There have been no additional interior points used in the computations. (b) The computed matrix condition number for the full

solution matrix (solid) and uncoupled single-scatter matrix (dashed). For both plots, the vertical lines indicate the predicted locations of the eigenfrequencies of the interior Dirichlet problem.

Figure 6 - A comparison of the computed backscattered spectra using the cylindrical BIEM with the full solution (solid lines) and the single-scatter solution (markers) for source/receiver 45° (circles), 60° (diamonds), and 90° (+) off the vertical axis below the cylinder. The cylinder is tilted at -45° with respect to the horizontal. For clarity, the symbols are shown at every fifth frequency value. The full-scattering solution for 90° is the line near the vertical centre of the plot which appears unassociated.

Figure 7 - The computed echo time series for a 2500-Hz Ricker wavelet using the full solution (solid line) and the single-scatter solution (dashed) for: (a) 45° off the vertical, (b) 60° off the vertical and (c) 90° off the vertical.

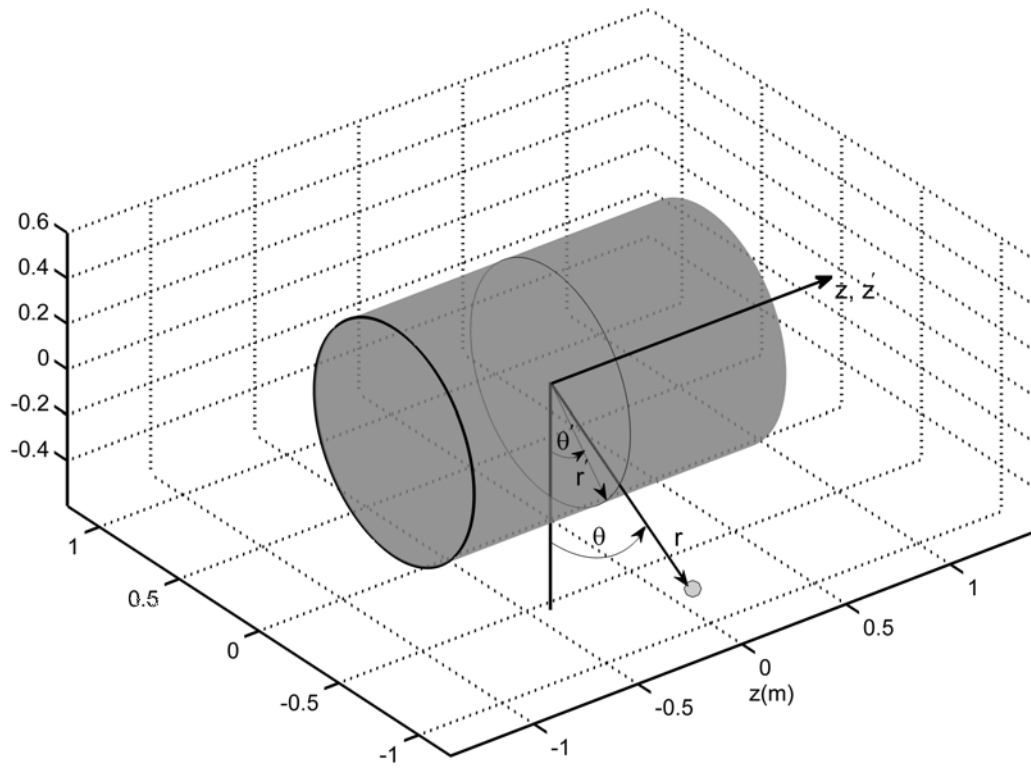


Figure 1: Schematic drawing of a 1.5m long cylinder with radius 0.5. A generic receiver position is shown at $(r, \theta, z = 0)$. A point on the surface at $(r' = 0.5, \theta', z' = 0)$ is also shown.

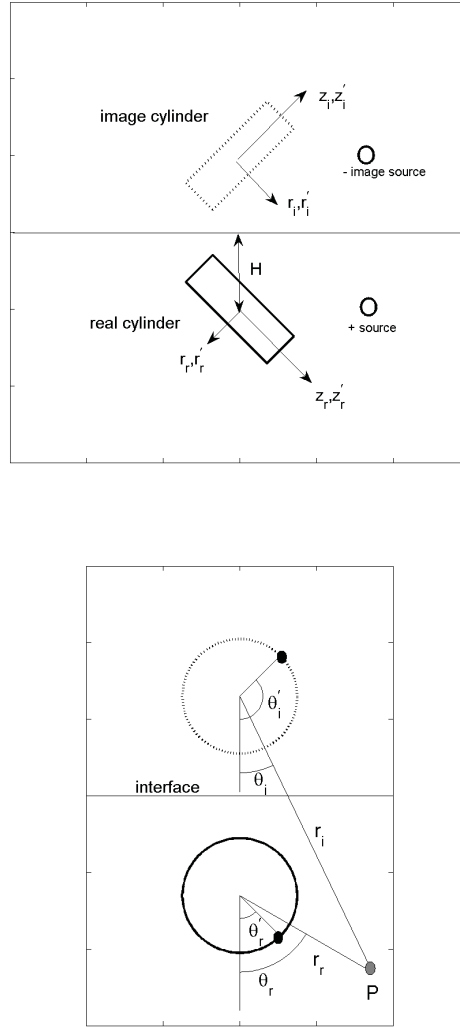


Figure 2: Schematic drawings of geometry and notation for (upper) tilted cylinder with a source and the mirror image. The tilted cylinder has a centre offset H . (lower) The angular coordinate system is shown on the endcaps of a cylinder lying parallel to the interface. A receiver point P is indicated with the angles θ_r and θ_i the azimuthal angles measured from the lower and image cylinders, respectively.

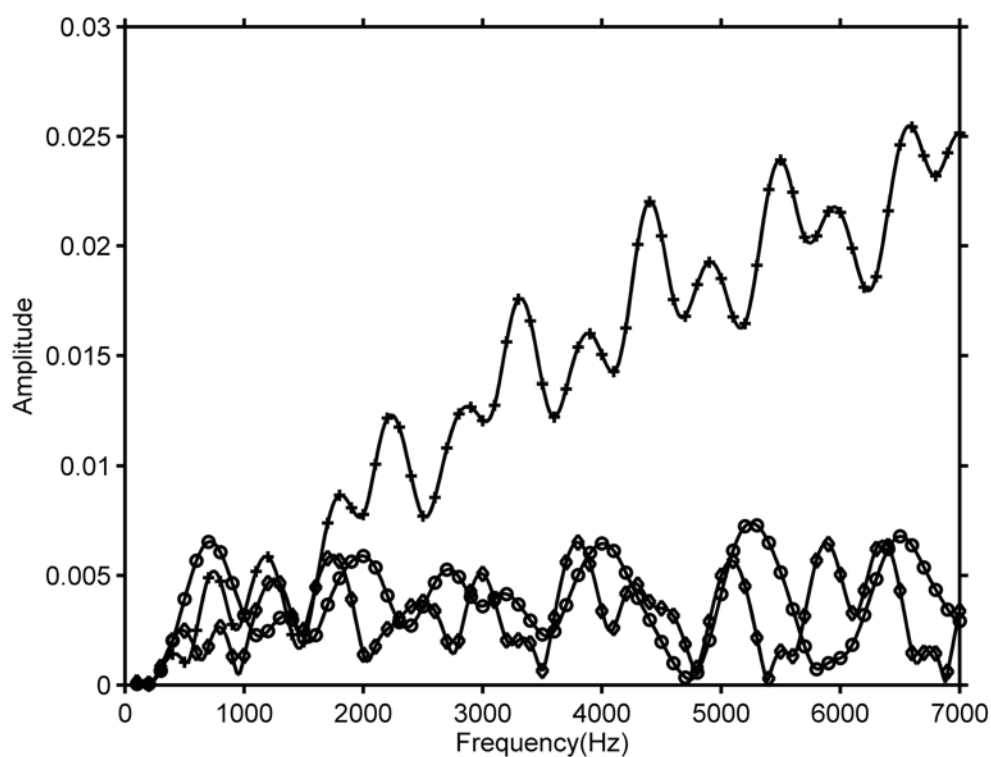


Figure 3: A comparison of the computed backscattered spectra using the virtual source technique (solid lines) and the cylindrical BIEM (markers) for source/receiver 60° (circles), 30° (diamonds), and 0° (+) off the vertical axis below the sphere. For clarity, the symbols are shown at every fifth frequency value.

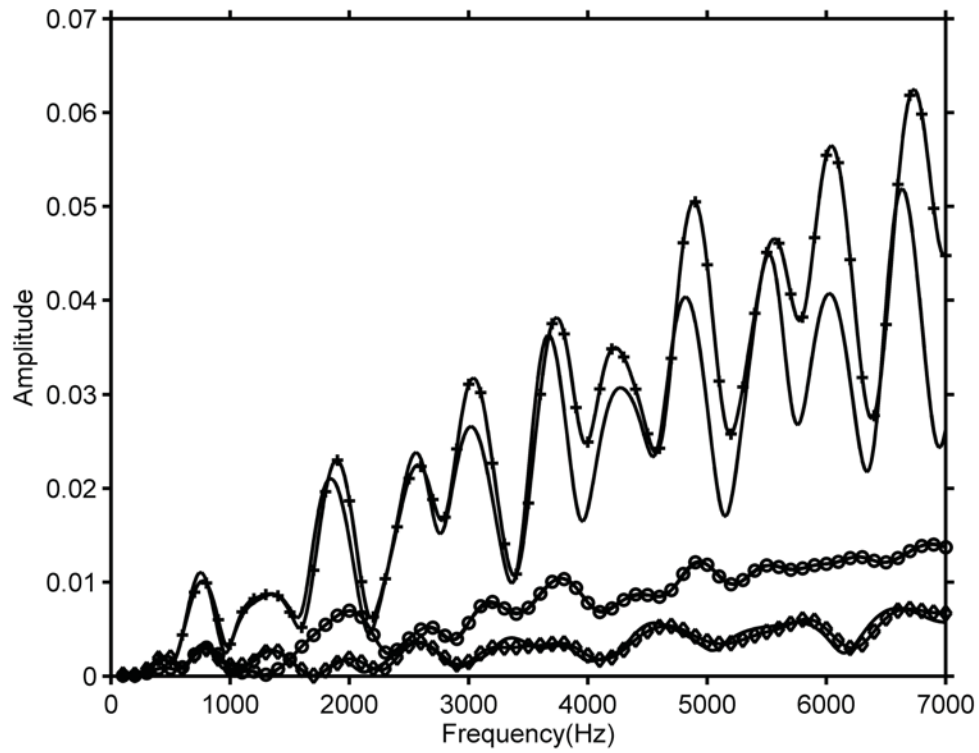


Figure 4: A comparison of the computed backscattered spectra using the cylindrical BIEM with the full solution (solid lines) and the single-scatter solution (lines with markers) for source/receiver 60° (circles), 30° (diamonds), and 0° (+) off the vertical axis below the cylinder. For clarity, the symbols are shown at every fifth frequency value.

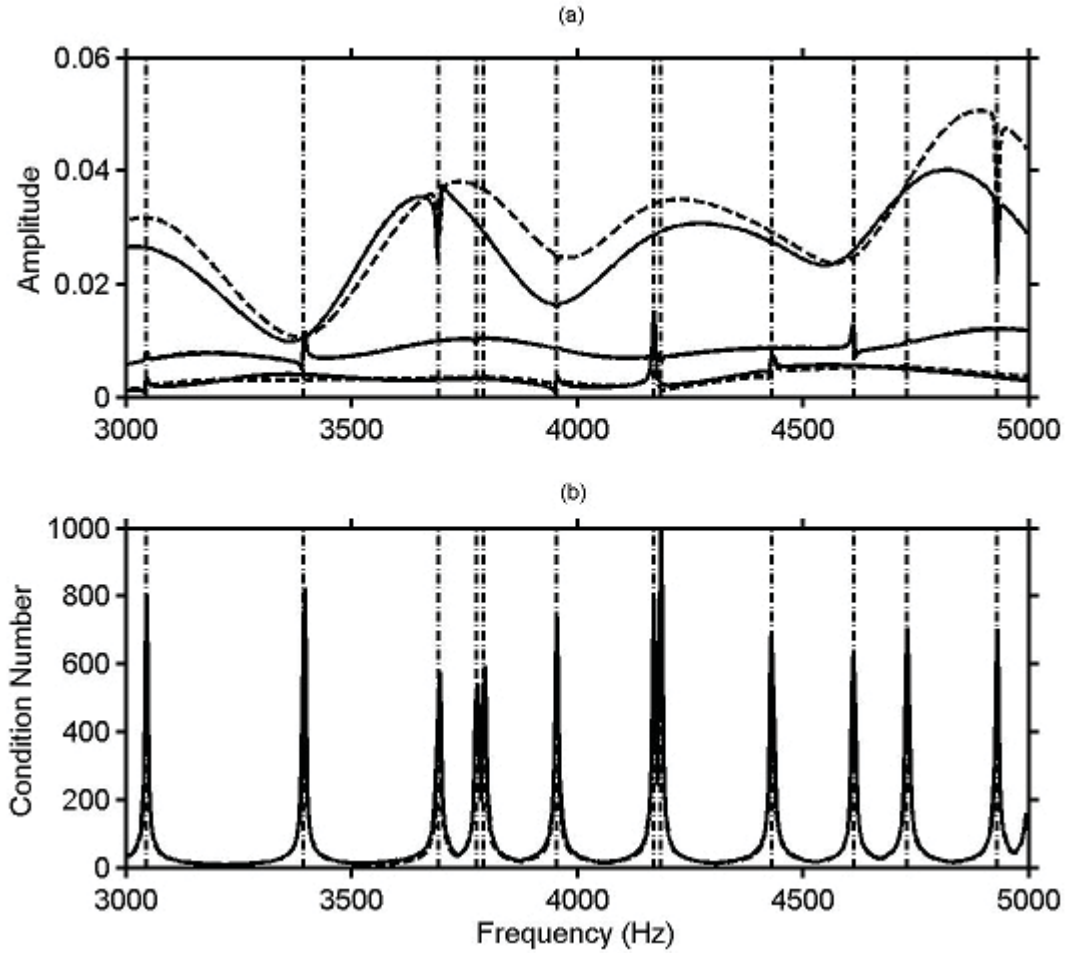


Figure 5: (a) The computed backscattered spectral amplitude for the source/receiver configurations of Fig. 4 using full solution (solid) and single-scatter solutions (dashed). There have been no additional interior points used in the computations. (b) The computed matrix condition number for the full solution matrix (solid) and uncoupled single-scatter matrix (dashed). For both plots, the vertical lines indicate the predicted locations of the eigenfrequencies of the interior Dirichlet problem.

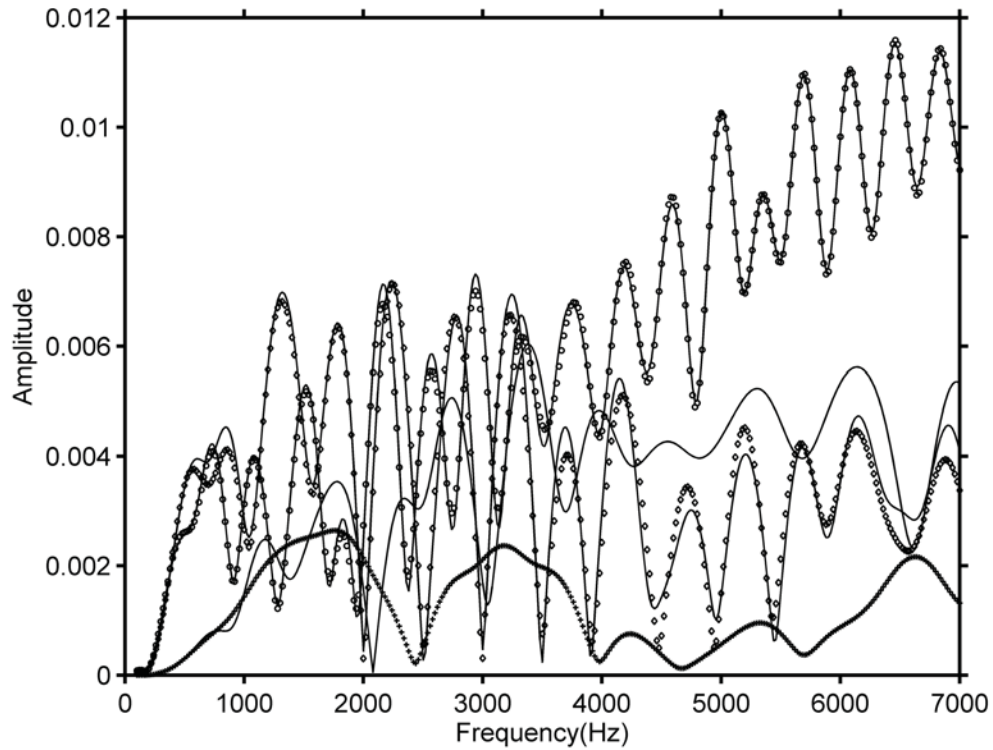


Figure 6: A comparison of the computed backscattered spectra using the cylindrical BIEM with the full solution (solid lines) and the single-scatter solution (markers) for source/receiver 45° (circles), 60° (diamonds), and 90° (+) off the vertical axis below the cylinder. The cylinder is tilted at -45° with respect to the horizontal. For clarity, the symbols are shown at every fifth frequency value. The full-scattering solution for 90° is the line near the vertical centre of the plot which appears unassociated.

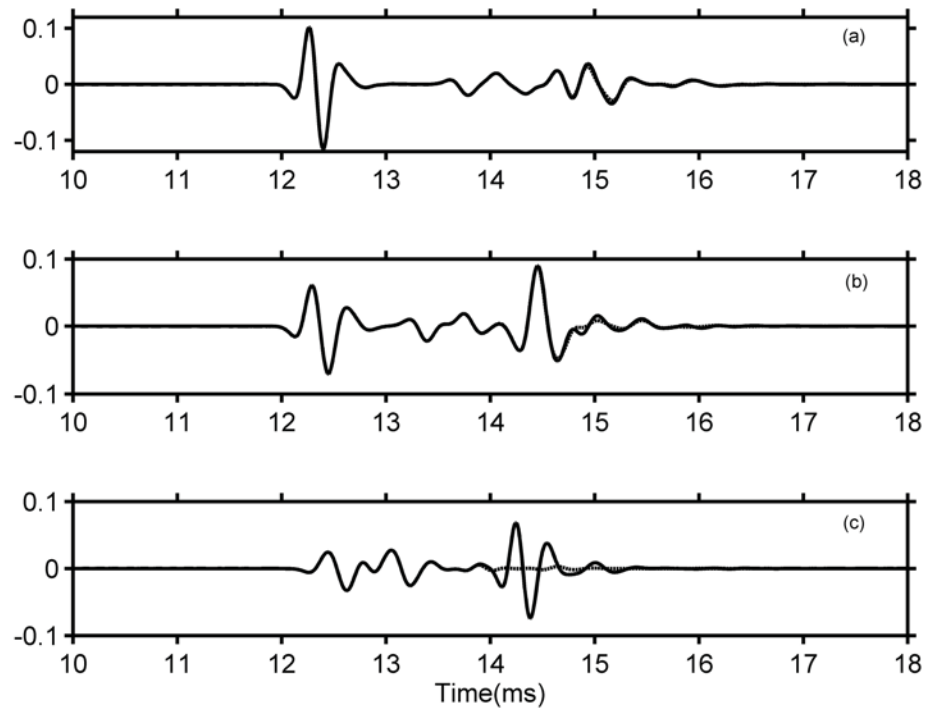


Figure 7: The computed echo time series for a 2500-Hz Ricker wavelet using the full solution (solid line) and the single-scatter solution (dashed) for: (a) 45° off the vertical, (b) 60° off the vertical and (c) 90° off the vertical.